Understanding the High Activity of Fe−N−C Electrocatalysts in Oxygen Reduction: Fe/Fe$_3$C Nanoparticles Boost the Activity of Fe−N$_x$

Wen-Jie Jiang,[†,‡] Lin Gu,[§] Li Li,[‡] Yun Zhang,[†,‡] Xing Zhang,[†] Lin-Juan Zhang,[∥] Jian-Qiang Wang,[∥] Jin-Song Hu,*[†] Zidong Wei,*[‡] and Li-Jun Wan*[†]

[†]Beijing National Laboratory for Molecular Sciences, Key Laboratory of Molecular Nanostructure and Nanotechnology, Institute of Chemistry, University of Chinese Academy of Sciences, Beijing 100190, China

[‡]State Key Laboratory of Power Transmission Equipment and System Security and New Technology, College of Chemistry and Chemical Engineering, Chongqing University, Chongqing 400044, China

[§]Beijing National Laboratory for Condensed Matter Physics, Collaborative Innovation Center of Quantum Matter, Institute of Physics, Chinese Academy of Sciences, Beijing 100190, China

[∥]Shanghai Synchrotron Radiation Facility, Shanghai Institute of Applied Physics, Chinese Academy of Sciences, Shanghai 201800, China

S *Supporting Information*

ABSTRACT: Understanding the origin of high activity of Fe−N−C electrocatalysts in oxygen reduction reaction (ORR) is critical but still challenging for developing efficient sustainable nonprecious metal catalysts in fuel cells and metal−air batteries. Herein, we developed a new highly active Fe−N−C ORR catalyst containing Fe−N$_x$ coordination sites and Fe/Fe$_3$C nanocrystals (Fe@C-FeNC), and revealed the origin of its activity by intensively investigating the composition and the structure of the catalyst and their correlations with the electrochemical performance. The

detailed analyses unambiguously confirmed the coexistence of Fe/Fe$_3$C nanocrystals and Fe−N$_x$ in the best catalyst. A series of designed experiments disclosed that (1) N-doped carbon substrate, Fe/Fe$_3$C nanocrystals or Fe−N$_x$ themselves did not deliver the high activity; (2) the catalysts with both Fe/Fe$_3$C nanocrystals and Fe−N$_x$ exhibited the high activity; (3) the higher content of Fe−N$_x$ gave the higher activity; (4) the removal of Fe/Fe$_3$C nanocrystals severely degraded the activity; (5) the blocking of Fe−N$_x$ downgraded the activity and the recovery of the blocked Fe−N$_x$ recovered the activity. These facts supported that the high ORR activity of the Fe@C-FeNC electrocatalysts should be ascribed to that Fe/Fe$_3$C nanocrystals boost the activity of Fe−N$_x$. The coexistence of high content of Fe−N$_x$ and sufficient metallic iron nanoparticles is essential for the high ORR activity. DFT calculation corroborated this conclusion by indicating that the interaction between metallic iron and Fe−N$_4$ coordination structure favored the adsorption of oxygen molecule. These new findings open an avenue for the rational design and bottom-up synthesis of low-cost highly active ORR electrocatalysts.
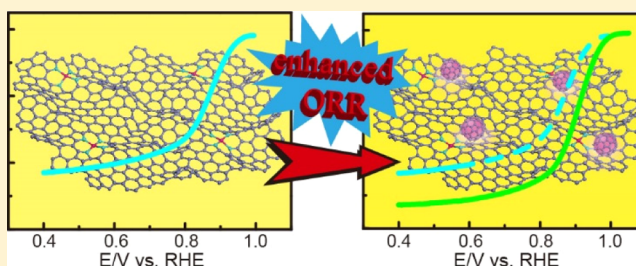
1. INTRODUCTION

The electrochemical reduction of oxygen is the pivotal step in controlling the performance of various next-generation energy conversion and storage devices, such as fuel cells, metal−air batteries and certain electrolyzers.[1−4] The commercialization of these technologies prominently depends on the development of low-cost high-performance electrocatalysts for oxygen reduction reaction (ORR). Currently, the most efficient and widely used ORR catalysts are precious metal group (PMG) materials.[5,6] The prohibitive cost and scarcity of the precious metals has stimulated extensive exploration of alternative low-cost nonprecious metal catalysts (NPMCs) with attractive performance for the ORR.[7] A variety of NPMCs with high activity and stability have been reported in recent years.[8−19] To warrant implementation in

practical energy conversion and storage devices, it is highly desirable but still challenging to create highly active, stable and low-cost catalysts with superior activity even over commercial Pt/C catalyst.

Among various alternative NPMCs, the materials containing transition metal−nitrogen coordination sites (M−N$_x$, M = Fe, Co, etc.) have been generally considered to be the most promising substitutes for PMG catalysts. Studies on these typical catalysts were initiated by the discovery of the ORR activity of cobalt phthalocyanine reported by Jasinski in 1964,[20] followed by the investigation of its analogues (metal−nitrogen coordinating

macrocycles) to improve their catalytic activities.[21−26] Due to the high cost of these metal macrocycles, the situation had a marginal success until Yeager proposed a model that electronically conducting surfaces with nitrogen groups were capable of binding transition metal species to form M-N$_x$ structure.[27] Thus, this model provided an economic method for the facile preparation of Fe−N−C catalysts through the pyrolysis of inorganic iron salts, carbon and nitrogen sources. Since then, great progress has been made in this field.[28−34] In spite of a few significant advancements achieved by delicate selection of suitable transition metal, nitrogen and carbon precursors and optimization of the nanostructing process,[12,24,30,35−41] the ORR performance of NPMCs still need to be further improved.

Besides the activity, the nature of active sites responsible for high activity in Fe−N−C catalysts still remains elusive to date, although intensive efforts had been attempted to reveal it by using physical or electrochemical techniques.[36,42−52] There is a general agreement that Fe is playing important role in enhancing the ORR activity of the catalysts. Recently, trace amount of transition metals were reported to significantly affect the ORR catalytic activity of metal-free catalysts.[53,54] Tremendous progress has been made for pyrolyzed Fe−N−C catalysts,[29,30,36,41,55−59] several of which exhibit superior performance for oxygen electroreduction.[12,33,34,60] However, there are still debates on what are the real active sites and whether Fe only promotes the formation of active sites or directly participates in catalyzing ORR.[36] Up to now, almost no clear and solid evidence was observed or intense investigation was done to unveil how the introduction of Fe boosts the catalytic activity of Fe−N−C catalysts for ORR, except for a few discussion reported very recently.[48,49] The lack of knowledge about active sites, caused by the low density of active sites and the complexity of both structure and composition in these Fe−N−C catalysts, has greatly hampered the rational design and preparation of high active and durable Fe−N−C catalysts.

Herein, we reported a facile and easily scalable method to prepare a highly active Fe−N−C ORR catalyst (Fe@C-FeNC) which contains Fe-N$_x$ configurations and graphene-encapsulated Fe/Fe$_3$C (Fe@C) nanocrystals. The catalyst exhibited superior catalytic activity for ORR with a half-wave potential $E_{1/2}$ of 0.899 V (all potentials used in the context are versus to reversible hydrogen electrode (RHE)) in 0.1 M KOH solution, which is 15 mV higher than that of commercial Pt/C, and a kinetic mass current of 41.6 A/g at 0.8 V. It was found that the pyrolysis process not only created the Fe-N$_x$ configurations, but also aggregated iron atoms to form graphene-encapsulated metallic Fe/Fe$_3$C nanocrystals around Fe-N$_x$ species. More interestingly, the in-depth investigation on morphology, composition and local structure of the catalysts unambiguously disclosed that these Fe@C nanocrystals dramatically boosted the catalytic activity of the neighboring Fe-N$_x$ active sites for ORR, which should be responsible for the enhanced performance. The high content of Fe-N$_x$ sites and sufficient Fe@C nanocrystals are essential to present the high catalytic activity for ORR. This finding sheds light on the origin of high catalytic performance of the Fe−N−C catalysts, and opens a path for rationally designing highly active ORR electrocatalysts.

2. RESULTS

The catalyst Fe@C-FeNC was prepared by coating carbon nanotubes (CNTs) with glucose in the presence of iron salt precursor, followed by the pyrolysis in the presence of melamine as nitrogen source. In order to investigate the effect of Fe content

on the morphology and catalytic performances of the catalysts, three Fe@C-FeNCs with different Fe contents were prepared. Compared with Fe@C-FeNC-1, three and five times amount of iron source were used to prepare Fe@C-FeNC-2 and −3, respectively (see Supporting Information for the details). Based on the thermogravimetric analysis (TGA, Figure S1), the final Fe contents in three catalysts are 2.57 wt % for Fe@C-FeNC-1, 4.42 wt % for Fe@C-FeNC-2, and 20.2 wt % for Fe@C-FeNC-3, respectively. It can be seen that the more iron source was used the more iron remained in the catalysts and the more carbon lost during preparation, causing the big difference of iron content between Fe@C-FeNC-2 and -3 catalysts. The transmission electron microscope (TEM) images of Fe@C-FeNC-2 in Figure 1a,b show that the catalyst consisted of coated CNTs and flocculent carbon nanostructures which should be resulted from the migration and rearrangement of carbon atoms catalyzed by active iron atoms during heat treatment.[34] Nanoparticles in several nanometers with darker contrast were clearly identified in both flocculent carbon nanostructures and coated CNTs. A close look at Figure 1b and the bright-field high-resolution TEM (HRTEM) image (Figure 1c and Figure S2) reveals that these nanoparticles were encapsulated with a few graphene layers and well crystallized with a lattice distance of 0.204 nm. When the amount of iron precursor decreased to one-third, the as-prepared catalyst (Fe@C-FeNC-1) comprised the flocculent, thin and wrinkled carbon nanostructures connected with CNTs as shown in Figure 1d,e. No clear nanoparticles were found in whole TEM observation. While the amount of iron precursor increased in the preparation of Fe@C-FeNC-3, the larger nanoparticles in around 20 nm appeared (Figure 1f). HRTEM image in Figure 1g discloses that these nanoparticles were also crystallized with a lattice distance of 0.204 nm and encased with a few graphene layers. It should be noted that the nanoparticles in Figure 1b,f exhibited a size distribution since they were formed by the random aggregation of iron atoms at high temperature during pyrolysis.

In order to further identify the nature of these nanocrystals, X-ray diffraction patterns of three samples were recorded and presented in Figure 1h. The XRD pattern of Fe@C-FeNC-1 (red curve) shows a sharp peak at 26.1° and a board peak at 43.1°, both of which can be assigned to graphitic carbon. No other detectable peaks appear in the XRD pattern, implying that iron atoms might be incorporated into carbon framework in disordered form. As the amount of iron precursor increased, crystalline phases of metallic Fe, Fe$_3$C are detected in Fe@C-FeNC-2 and Fe@C-FeNC-3. Four diffraction peaks at 26.1°, 43.7°, 44.7° and 65.0° in the XRD pattern of Fe@C-FeNC-2 (green curve) can be indexed to the diffraction from (002) planes of graphite, (102) planes of Fe$_3$C (cementite, JCPDS No. 35−0772), and (110) and (200) planes of cubic Fe (JCPDS No. 06−0696), respectively. The relative diffraction intensity from Fe$_3$C increased as the iron content further increased in the XRD pattern of Fe@C-FeNC-3 (purple curve), indicating an increased ratio of Fe$_3$C/Fe. These results indicate that metallic Fe, Fe$_3$C and graphitic carbon coexisted in the catalyst Fe@C-FeNC-2 and Fe@C-FeNC-3. Taking into account the TEM results together, the nanoparticles in both Fe@C-FeNC-2 and Fe@C-FeNC-3 should be Fe/Fe$_3$C nanocrystals. The continuous lattice distance of 0.204 nm in Figure 1c,g is well consistent with the d-spacing of (220) crystallographic planes of Fe$_3$C or (110) planes of cubic Fe. According to the knowledge on in situ growth of CNTs,[61−63] it can be inferred that the Fe/Fe$_3$C nanocrystals should originate from the reduction of iron precursor by carbon during pyrolysis.
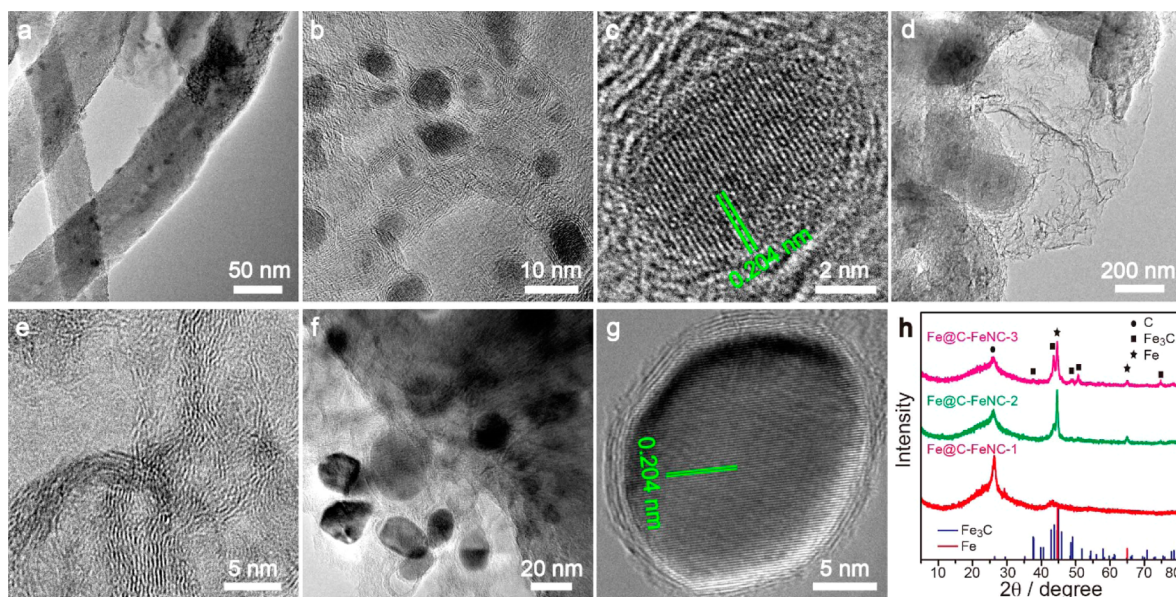
Figure 1. (a,b) TEM and (c) HRTEM images of Fe@C-FeNC-2. (d,e) TEM images of Fe@C-FeNC-1. (f) TEM and (g) HRTEM images of Fe@C-FeNC-3. (h) XRD patterns of three Fe@C-FeNC catalysts as well as Fe (JCPDS No. 06−0696, red vertical line) and Fe$_3$C (JCPDS No. 35−0772, blue vertical line) as references.

While the composite containing iron compound and carbon or carbonaceous materials was pyrolyzed at high temperature, iron compound was reduced by carbon to metallic iron. These metallic Fe atoms are chemically extremely active to react with other atoms such as nitrogen or catalytically graphitize carbon planes. If the Fe concentration is low enough (the case of Fe@C-FeNC-1), most of Fe atoms involved in the formation of graphene-like graphitic layers or reacted with nitrogen atoms to generate the Fe−N$_x$ species before they aggregated. When the Fe concentration increased in the case of Fe@C-FeNC-2, the excessive Fe will aggregate to form Fe nanocrystals, which subsequently produce carbides with carbon atom and catalytically graphitize carbon to generate graphene-like carbon layer surrounding the nanocrystals during the pyrolysis and cooling. As the dosage of iron precursor further increases in the case of Fe@C-FeNC-3, Fe nanocrystals grow up. The larger size of Fe nanocrystals makes the inside carbon atoms difficult to diffuse onto the outer surface, thus creating more Fe$_3$C phase as indicated in XRD patterns.

The catalytic activity for ORR of the prepared catalysts was first assessed using rotating ring-disk electrode (RRDE) in 0.1 M KOH solution saturated with O$_2$, and compared with commercial Johnson Matthey Pt/C (20% Pt loading) catalyst. In order to better understand the catalytic performances and reveal the active sites in the catalyst Fe@C-FeNCs, three control catalysts were prepared by the same synthetic route as Fe@C-FeNC-2 except for no addition of iron source, nitrogen source (melamine), and both iron source and melamine, noted as NC, Fe@C, and C respectively. As shown in TEM images (Figure S3a,b), only carbon nanotubes with porous carbon layer derived from the pyrolysis of polymerized glucose coating exist in the catalyst NC. No flocculent carbon nanostructure or nanoparticles were found in the catalyst NC since no iron was introduced as the catalyst to form these structures. The TEM images (Figure S3c,d) and XRD pattern (see Figure S4b) demonstrated that the control catalyst Fe@C has similar morphology and composition to Fe@C-FeNC-2 but the Fe/

Fe$_3$C nanoparticles are larger probably due to no consumption in the formation of FeN$_x$ unlike Fe@C-FeNC-2.

The linear sweep voltammetry (LSV) results (red curve in Figure 2a) indicate that the control catalyst C (porous carbon coated carbon nanotubes without N-doping and iron) shows the worst ORR activity in terms of the most negative $E_{1/2}$. After the introduction of iron alone, the catalyst Fe@C shows very little improvement on activity, implying that Fe/Fe$_3$C nanoparticles themselves show similar catalytic activity to the pristine carbon materials in alkaline medium. The poor activity of the control catalyst C and Fe@C are further disclosed by a high hydrogen peroxide yield of approximate 50% and 40% at 0.75 V (Figure 2b), corresponding to the electron transfer number of 2.9 and 3.1 which are calculated on a basis of currents on disk and ring electrodes, respectively (Figure 2c). This result suggests that the ORR processes on the catalyst C and Fe@C dominate by a 2-electron reduction pathway. In contrast, when the nitrogen was introduced into the catalyst, the metal-free control catalyst NC exhibits an apparently enhanced catalytic activity for ORR in view of an $E_{1/2}$ at 0.787 V, 62 mV higher than the catalyst Fe@C. The decreased hydrogen peroxide (H$_2$O$_2$) yield corroborates the improvement of ORR performance after the incorporation nitrogen in the catalyst. This improvement could be safely attributed to the effect of nitrogen doping in carbon materials, as reported in the literature.[34,60] However, it is noteworthy that while both iron and nitrogen were introduced into the catalyst the ORR activity of the catalyst Fe@C-FeNC-2 tremendously leaped forward in terms of a remarkably positively shifted $E_{1/2}$ at 0.899 V, which is 212 and 112 mV positive than that of the catalysts Fe@C and NC, respectively. The larger limited current density implies that the conductivity of the catalyst was improved, which could be ascribed to the improvement of graphitization in the presence of iron and nitrogen during pyrolysis. Such an $E_{1/2}$ is 15 and 7 mV positive than those of commercial Pt/C (Johnson-Matthey, 20 wt %) at 0.884 V and Pd/C (Johnson-Matthey, 20 wt %) at 0.892 V (Figure S5), respectively, indicating the catalyst Fe@C-FeNC-2 demonstrates the better ORR activity than commercial Pt/C and Pd/C. This is
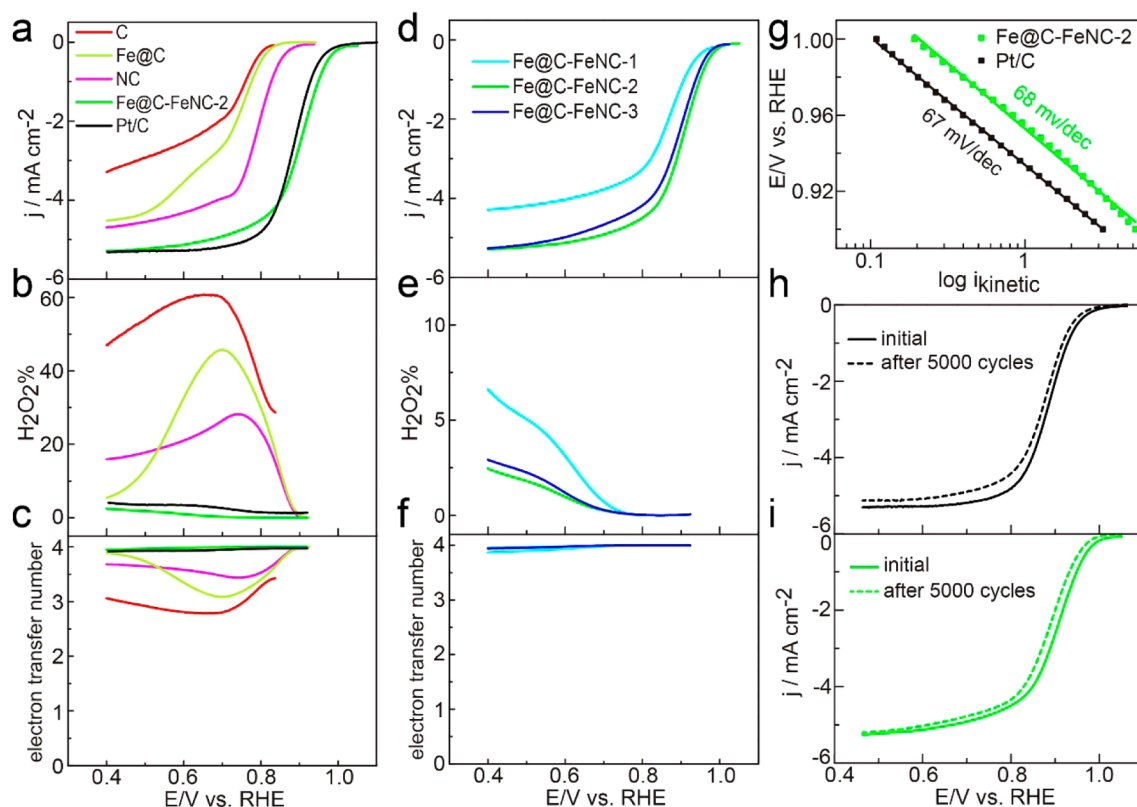
Figure 2. (a,d) Steady-state ORR polarization curves, (b,e) hydrogen peroxide yield and (c,f) corresponding electron transfer number during ORR process. (g) Tafel plots of Fe@C-FeNC-2 and Pt/C. (h,i) Steady-state ORR polarization curves of Pt/C (h) and Fe@C-FeNC-2 (i) before and after 5000 potential cycles in O_2-saturated in 0.1 M KOH. The loading of all nonprecious catalysts is 700 μg/cm^2.

one of the highly active non-Pt catalysts with ORR performance better than Pt/C.[11,12] The RRDE measurement reveals that the evolution of hydrogen peroxide is strikingly suppressed on the catalyst Fe@C-FeNC-2. H_2O_2 yield is lower than 2.5% over the scanned potential range as shown in Figure 2b and apparent smaller than that on Pt/C. Specifically, the H_2O_2 yield on Fe@C-FeNC-2 at $E_{1/2}$ is less than 0.01% compared with 1.31% on Pt/C. Figure 2c displays that the electron transfer number during the reaction is 3.95−3.99 for Fe@C-FeNC-2 over the scanning range of potentials, indicating that ORR process on Fe@C-FeNC-2 ideally follows the four electron pathway. Therefore, the above results reveal that it is essential to simultaneously introduce both iron and nitrogen into the catalyst for achieving such significant improvement on the ORR activity, which could produce intrinsically different active sites, such as iron−nitrogen coordinating species (Fe−N$_x$).

The effect of the dosage and the state of introduced iron on the electrocatalytic activity of Fe@C-FeNCs catalysts was further explored. As shown in Figure 2d, the catalyst Fe@C-FeNC-2 shows the best performance in terms of the most positive $E_{1/2}$ of 0.899 V and the highest kinetic mass current of 41.6 A/g at 0.80 V. In contrast, the catalyst Fe@C-FeNC-1 exhibits the degraded ORR activity with a $E_{1/2}$ of 0.862 V while the catalyst Fe@C-FeNC-3 also shows slightly degraded ORR activity with a $E_{1/2}$ of 0.885 V. The RRDE measurements corroborate that Fe@C-FeNC-1 shows the worst activity for ORR among three catalysts in terms of the highest yield of H_2O_2 although it still beats the control catalysts C, Fe@C and NC (Figure 2e). The electron transfer number for all three Fe@C-FeNC catalysts are approaching the ideal value of 4.0 (Figure 2f). Furthermore, it is known that in order to obtain a high current at low

overpotential for an electrochemical reaction, the reaction should exhibit a low Tafel slope.[64] As shown in Figure 2g, Tafel slope of ∼68 mV/dec for Fe@C-FeNC-2 is very close to that of ∼67 mV/dec for Pt/C. This means that the transfer of the first electron is probably the rate-determining step in ORR catalyzed by Fe@C-FeNC-2, similar to platinum.[65] The durability of catalyst was subsequently assessed using the accelerated durability test protocol from the US Department of Energy by cycling the catalysts between 0.6 and 1.0 V at 50 mV s^{-1} under O_2 atmosphere. After 5000 continuous cycles, the $E_{1/2}$ on Fe@C-FeNC-2 negatively shifts by ∼16 mV (Figure 2h), slightly larger than 10 mV on Pt/C (Figure 2i). Lastly, it is worth noting that the concept demonstrated in this manuscript is not limited to using carbon nanotubes as the active site carrier. For example, in consideration of the cost and mass production of the catalyst, the cheap acetylene black (AB) was used to substitute for CNTs in the preparation of Fe@C-FeNC-2. the resulting catalyst shows a good ORR activity as well in terms of a $E_{1/2}$ of 0.888 V (Figure S6), which is comparable to Pt/C.

The electrochemical measurements show that both iron and nitrogen are playing important role in enhancing the ORR activity and the amount of iron significantly affect the performance of the catalysts. In order to reveal the status of iron and nitrogen in the catalysts, an aberration-corrected scanning transmission electron microscopy (AC-STEM) equipped with an electron energy loss spectrometer was applied to analyze high-resolution elemental distribution. Figure 3a shows the annular bright field (ABF) STEM images of the catalyst Fe@C-FeNC-1. Only flake-like structures were found, which are similar to graphitic carbon structures observed under conventional TEM observation in the literatures.[41,58] But in
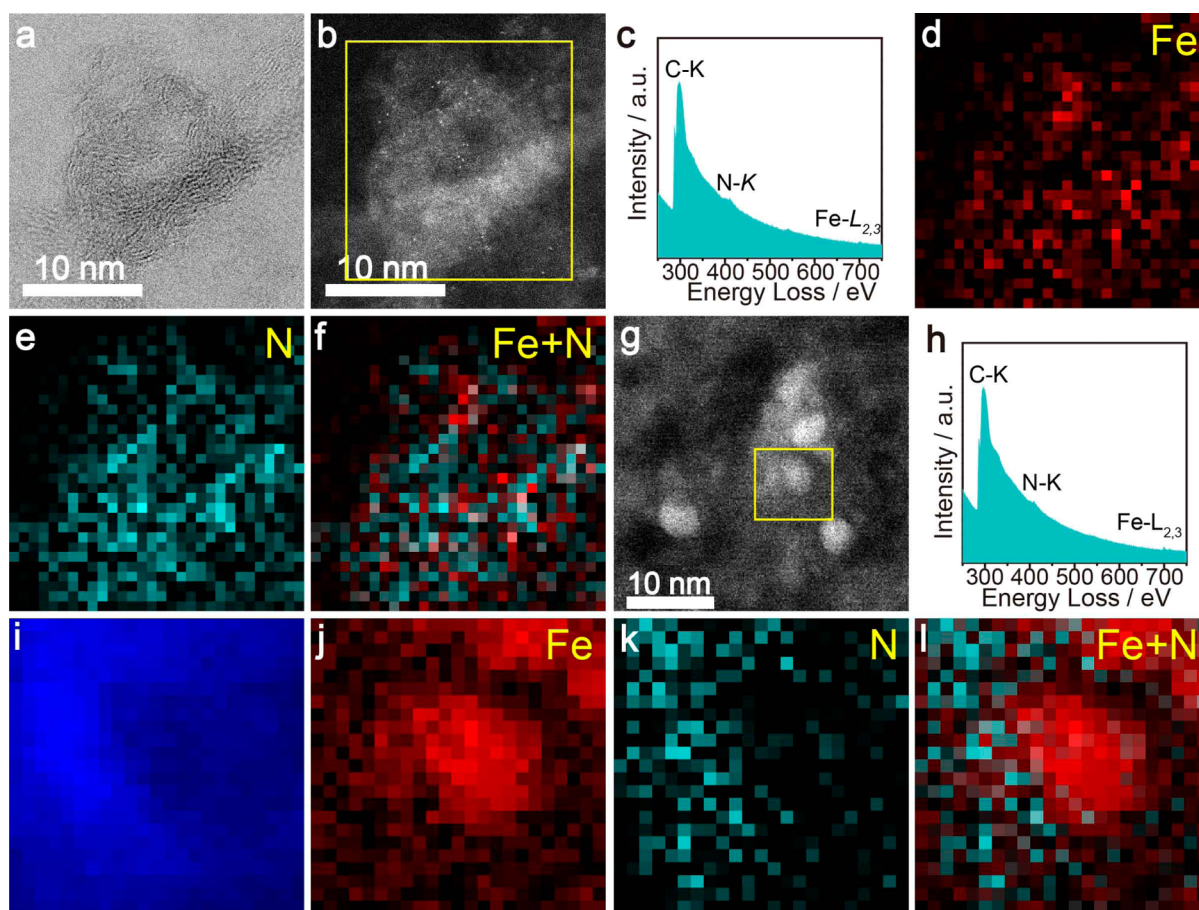
Figure 3. (a) ABF image, (b) HAADF STEM image, (c) EELS spectrum, (d–f) EELS mapping of iron, nitrogen, and overlaid iron and nitrogen of the area marked by yellow square in (b) for Fe@C-FeNC-1 sample. (g) HAADF STEM image, (h) EELS spectrum, (i–l) EELS mapping of carbon, iron, nitrogen, and overlaid iron and nitrogen of the area marked by yellow square in (g) for Fe@C-FeNC-2.

high-angle annular dark field (HAADF) mode (Figure 3b), a number of bright spots in a size at atomic scale unambiguously appear, which should correspond to the heavy atoms. Iron and nitrogen atoms were further identified and mapped out by electron energy loss spectroscopy (EELS) analysis (Figure 3c–f). The signals of carbon, nitrogen and iron are distinguishable in EELS spectrum. The overlay of iron and nitrogen signals in the elemental mapping images (Figure 3f) clearly discloses that iron atoms are adjacent to nitrogen atoms at atomic level, suggesting the presence of Fe–N$_x$ coordination. On the other hand, nanoparticles appear in the HAADF STEM image (Figure 3g) of the catalyst Fe@C-FeNC-2. EELS mapping images (Figure 3j–l) confirm that these nanoparticles are iron aggregations, which are surrounded with iron and nitrogen atoms at atomic level. This result suggests the existence of Fe–N$_x$ closely adjacent to iron nanoparticles in Fe@C-FeNC-2. Such environment would allow for the interaction of iron nanoparticles and Fe–N$_x$.

In attempt to further understand the nature of ORR catalytically active sites, X-ray absorption spectroscopy at Fe k-edge, a sensitive characterization for identifying noncrystalline species, was conducted to analyze the coordination environment of iron. Figure 4a shows the k3 weighted Fourier transformation of Fe K edge from extended X-ray absorption fine structure (EXAFS) spectra for commercial iron phthalocyanine (FePc) and iron foil as the references as well as three Fe@C-FeNCs. Quantitative information on the local structures was obtained by fitting EXAFS data using the IFEFFIT package and listed in

Supporting Information (Table S1). The fitting curves are plotted in Supporting Information (Figure S7). It can be seen from Figure 4a that all Fe@C-FeNCs exhibit peaks at 1.44 ± 0.06 Å assigned to Fe–N distance due to a nitrogen shell surrounding Fe in reference to that of FePc, corroborating the existence of the Fe–N$_x$ coordination.[34,66] Another peak at 2.46 ± 0.02 Å, ascribed to the Fe–C distance of the second neighbor shell in FePc, is clearly distinguished in the spectra of Fe@C-FeNC-1 and Fe@C-FeNC-2. These information suggests that Fe–N$_x$ configurations may be incorporated in the graphitic carbon frameworks in both catalysts, resulting in relative long-range order structure. Whereas, the spectrum of Fe@C-FeNC-3 is more like that of Fe foil with two strong peaks at 2.09 ± 0.13 Å and 4.46 ± 0.11 Å, which correspond to the Fe–Fe distance, referring to Fe foil. The peak of the Fe–Fe bond could also be observed in Fe@C-FeNC-2 although it is much weaker than that in Fe@C-FeNC-3. These results corroborate that metallic iron exists in both Fe@C-FeNC-2 and Fe@C-FeNC-3, which are consistent with the TEM and AC-STEM results. Moreover, it is noticed that the Fe–N peak in Fe@C-FeNC-3 is the weakest one among three catalysts, indicating the long-range order of Fe–N environment is weaker than other two. Together with the enhanced long-range order of Fe–N in Fe@C-FeNC-2 than that in Fe@C-FeNC-1 in terms of the stronger Fe–N signal, it could be inferred that the appropriate amount of iron benefits the long-range order of Fe–N environment, but the excessive amount of iron deteriorates it probably due to the high activity of iron
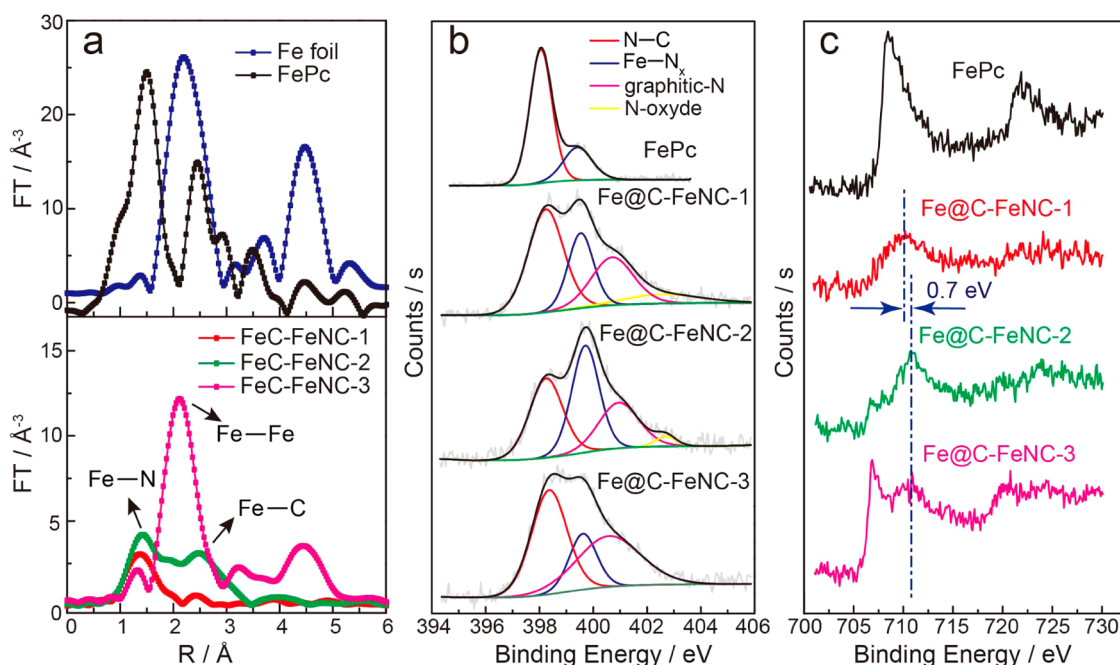
Figure 4. (a) Experimental Fourier transform at the Fe K-edge of EXAFS data of three Fe@C-FeNCs, and FePc and iron foil as references. (b) The deconvoluted N 1s spectra of FePc and three Fe@C-FeNC catalysts. (c) The Fe 2p narrow scan spectra of FePc and three FeC-FeNCs catalysts.

during pyrolysis. This is consistent with the XPS results mentioned thereinafter. In consideration of the ORR activity order (highest for Fe@C-FeNC-2, lowest for Fe@C-FeNC-1, Figure 2d), it revealed that the catalytic activity of the catalyst Fe@C-FeNC is not simply correlated with coordination environment of Fe−N.

X-ray photoelectron spectroscopy (XPS) was further performed for all three catalyst Fe@C-FeNCs and pure FePc as a reference to analyze the bonding state of iron and nitrogen (Figure 4b,c). The N 1s curve of FePc (Figure 4b) patently shows two peaks at 398.06 and 399.42 eV, corresponding to two distinct nitrogen bonding environments as marked in Supporting Information (Figure S8). The lower one is assigned to four nitrogen atoms located in N-substituted methine environment, an analogous configuration to meso-aza nitrogen structure in porphyrin, named as N−C configuration.[67] The higher one can be safely indexed to another four nitrogen atoms coordinated to iron atom, corresponding to Fe−N_x coordination. N 1s signals of Fe@C-FeNCs were deconvoluted as shown in Figure 4b and the results were elaborated in Supporting Information (see Table S2). The apparent peaks at around 399.57 eV in all three Fe@C-FeNCs confirm the presence of N similar to Fe−N_x moiety in FePc, which agrees with EXAFS results. The signals at around 398.22 and 400.74 eV can be attributed to the N with a chemical state similar to the above-mentioned N−C and graphitic nitrogen, respectively. Since the Fe−N_x sites are considered to be responsible for the high catalytic activity, the amount of nitrogen corresponding to Fe−N_x structures was calculated on a basis of total nitrogen content and its fraction in the catalysts. As shown in Table S2, this value is 1.956 at. % in Fe@C-FeNC-1, slightly decreases to 1.893 at. % in Fe@C-FeNC-2, and further decreases to 1.423 at. % in Fe@C-FeNC-3 with increasing iron content.

Taking into account the ORR activity order of the three catalysts, Fe@C-FeNC-1 with the highest amount of Fe−N_x but no Fe@C nanoparticles shows the lowest activity, while Fe@C-FeNC-3 with Fe@C nanoparticles but the lowest amount of Fe−

N_x exhibits the higher activity than Fe@C-FeNC-1. Fe@C-FeNC-2 with Fe@C nanoparticles and the higher amount of Fe−N_x than Fe@C-FeNC-3 delivers the highest activity. Together with the fact that Fe@C nanoparticles themselves shows negligible ORR activity (Figure 2a), it comes to a conclusion that Fe−N_x coordination should be the electrocatalytically active sites for ORR and Fe@C nanoparticles can dramatically promote the activity of the neighboring Fe−N_x for catalyzing ORR. Besides the analysis mentioned above, the binding state of Fe in these three catalysts gives another evidence of this promotion. As shown in XPS spectra (Figure 4c), the signal at 706.87 eV in the Fe 2p3/2 spectrum of Fe@C-FeNC-3 and 708.47 eV in FePc can be safely attributed to zero-valence Fe (metallic iron or carbide) and Fe^{2+}, respectively.[35] The signal at around 710 eV can be assigned to Fe in Fe−N_x configuration.[11] It is notable that the Fe peak of Fe−N_x configuration in Fe@C-FeNC-1 shifts by 0.7 eV (710.17 to 710.87 eV) to the higher binding energy in Fe@C-FeNC-2 and Fe@C-FeNC-3 (Figure 4c). This shift implies the less charge density on central Fe atoms, which is a clue of the interaction of Fe−N_x and Fe@C.

To further support the above conclusion, the two control experiments were carried out. (1) The catalyst Fe@C-FeNC-2 was leached in 0.5 M H_2SO_4 at 60 °C for 12 h to remove or substantially diminish metallic Fe nanoparticles. The TEM image in Supporting Information (Figure S9) confirms that almost no nanoparticles were found after the acid leaching. As a result, the acid-leached Fe@C-FeNC-2 shows apparently degraded ORR activity in terms of a much negatively shifted $E_{1/2}$ at 0.807 V, which is 92 mV lower than that of original Fe@C-FeNC-2. This result indicates that metallic Fe nanoparticles is necessary for the high ORR activity in Fe@C-FeNC-2. (2) It is known that SCN⁻ ion can poison Fe−N_x sites in catalyzing ORR.[36,68] In consideration of the potential reaction between SCN⁻ ion and KOH, we first measured the ORR activity of Fe@C-FeNC-2 in O_2-saturated 0.1 M $HClO_4$ containing 0.01 M NaSCN. It can be seen in Supporting Information (Figure S10) that the $E_{1/2}$ of Fe@C-FeNC-2 decreases significantly by about 111 mV after the
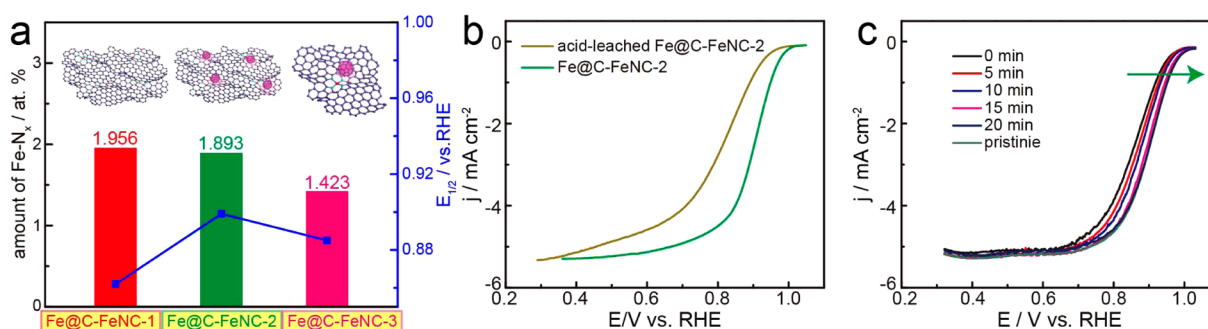
Figure 5. (a) The correlation between the amount of Fe−N_x coordination and catalytic ORR performances in terms of $E_{1/2}$ values for Fe@C-FeNCs. (b) Steady-state ORR polarization curves of as-prepared and acid-leached Fe@C-FeNC-2 measured in 0.1 M KOH. (c) Time-dependent steady-state ORR polarization curves of SCN⁻ poisoned Fe@C-FeNC-2 measured in 0.1 M KOH.

addition of 0.01 M NaSCN. The remarkably depression of catalytic activity can be attributed to the blocking of Fe−N_x active sites by SCN⁻ in catalyzing ORR. Moreover, if we pretreated the Fe@C-FeNC-2 electrode in 0.1 M HClO₄ containing 0.01 M NaSCN to partially block Fe−N_x sites, then rinsed it thoroughly with Milli-Q water and measured it in 0.1 M O₂-saturated KOH, we initially observed that the $E_{1/2}$ negatively shifted by 44 mV compared with that without treatment. However, the ORR LSV curve gradually recovered to its original position before the pretreatment of SCN⁻ since the blocked Fe−N_x sites gradually recovered as the dissociation of SCN⁻ on central iron sites in 0.1 M KOH (Figure 5c). This result unambiguously corroborates that Fe−N_x coordination sites should be responsible for the ORR activity of Fe@C-FeNCs. Therefore, these two control experiments strongly support the conclusion that the high content of Fe−N_x active sites and sufficient Fe@C crystals are essential to deliver high ORR catalytic performance.

The density functional theory (DFT) calculations revealed that the additional iron atom is able to provide extra electron to nitrogen atoms, resulting in the decrease of Mulliken charges on central iron atom of Fe−N_4 (Figure S11 and Table S3). After the modification by additional iron atom, the HOMO energy of the catalyst rises, leading to the more overlap with the LUMO of triplet O₂ molecule and thus the increase in activity for catalyzing ORR. In addition, the binding energy of O₂ with Fe-modified Fe−N_4 configuration is slightly higher than that of bare one, which favors the adsorption of O₂ on the active sites and thus promotes the ORR activity of Fe−N_4 configuration. The details of the calculation and the description were presented in the Supporting Information.

3. DISCUSSION

On the basis of the above results, we believe that the super catalytic activity of Fe@C-FeNC-2 can be attributed to the Fe−N_x sites promoted by neighboring Fe/Fe₃C nanoparticles. In fact, a few previously reported Fe−N−C catalysts which showed excellent ORR activity did feature both Fe−N_x sites and metallic Fe cluster or nanoparticles.[12,34,55−57,59,60,69,70] For example, Piotr Zelenay's group reported a N-doped CNT/nanoparticle composite with iron nanoparticles encapsulated in carbon shells as an efficient ORR electrocatalyst.[12] Although the paper did not discuss the origin of the high activity, it could be speculated that the two heat-treatment steps could create Fe−N_x configurations, which worked together with inner iron nanoparticles to lead to the high ORR activity of the catalyst. Dai's group synthesized CNTs-graphene complexes as ORR electrocatalysts by exfoliat-

ing the outer wall of few-walled CNTs via oxidation and high-temperature reaction with ammonia.[65] Atomic-scale microscopic observation suggested the existence of Fe−N_x sites and iron clusters were obviously found near to the Fe−N_x coordination, both of which should contribute to the enhanced electrocatalytic activity. This also can explain why some pyrolyzed Fe−N−C catalysts needed to be subjected to a second pyrolysis after acid treatment for removal of nonactive metal phase to keep good activity. The second annealing process would facilitate the residual irons to migrate together and form clusters or nanoparticles adjacent to Fe−N_x sites. Therefore, we proposed that the pyrolysis is not only the key step to create the Fe−N_x configurations, but also to aggregate iron atoms to form metallic clusters or nanoparticles, both of which contributed to the enhancement of catalytic performance. Besides, the concept could also interpret well the pyrolyzed metal macrocycles compounds are more active than the pristine ones.[7,27,71] Moreover, Bao's group experimentally and computationally demonstrated that coordinatively unsaturated Fe nanoclusters changed the charge-density distribution on outer N-doped carbon layers,[69] which is consistent with our result that metallic iron nanoparticles could change the charge density of central iron atom in Fe−N_x configuration and thus enhance its ORR activity.

4. CONCLUSION

In summary, a high-performance nonprecious metal catalyst for ORR was developed through a pyrolysis of the mixture of glucose coated carbon nanotubes, iron and nitrogen sources. The optimal catalyst Fe@C-FeNC-2 exhibited an ORR $E_{1/2}$ at 0.899 V, which is 15 mV higher than that of Pt/C. The analytical results from XRD, AC-TEM, EELS, EXAFS, and XPS confirm the coexistence of Fe/Fe₃C nanoparticles and Fe−N_x configuration in the catalyst. Taking into account the correlations between the content of Fe−N_x configuration and the ORR activities together with the EXAFS analysis, it unambiguously come to the conclusion that Fe@C nanoparticles can dramatically promote the activity of the neighboring Fe−N_x for catalyzing ORR. The more Fe−N_x sites in the presence of Fe@C nanoparticles will promise the higher ORR activity. This finding justifies why it is essential for the high ORR activity to have simultaneously metallic iron and nitrogen doping in the numerous reported carbon-based ORR catalysts[55−57,59,70] and may inspire the rational design of highly active ORR electrocatalysts for fuel cell and metal−air battery applications.

■ ASSOCIATED CONTENT

S **Supporting Information**

The Supporting Information is available free of charge on the ACS Publications website at DOI: 10.1021/jacs.6b00757.

Experimental section, supplementary figures and tables. (PDF)

■ AUTHOR INFORMATION

Corresponding Authors

*hujs@iccas.ac.cn
*zdwei@cqu.edu.cn
*wanlijun@iccas.ac.cn

Notes

The authors declare no competing financial interest.

■ ACKNOWLEDGMENTS

■ REFERENCES

(1) Steele, B. C. H.; Heinzel, A. *Nature* **2001**, *414*, 345.

(2) Debe, M. K. *Nature* **2012**, *486*, 43.

(3) Cao, R.; Lee, J.-S.; Liu, M.; Cho, J. *Adv. Energy Mater.* **2012**, *2*, 816.

(4) Li, Q.; Cao, R.; Cho, J.; Wu, G. *Adv. Energy Mater.* **2014**, *4*, 1301415.

(5) Gasteiger, H. A.; Marković, N. M. *Science* **2009**, *324*, 48.

(6) Stamenkovic, V. R.; Fowler, B.; Mun, B. S.; Wang, G.; Ross, P. N.; Lucas, C. A.; Marković, N. M. *Science* **2007**, *315*, 493.

(7) Jaouen, F.; Proietti, E.; Lefevre, M.; Chenitz, R.; Dodelet, J.-P.; Wu, G.; Chung, H. T.; Johnston, C. M.; Zelenay, P. *Energy Environ. Sci.* **2011**, *4*, 114.

(8) Cheng, F.; Shen, J.; Peng, B.; Pan, Y.; Tao, Z.; Chen, J. *Nat. Chem.* **2011**, *3*, 79.

(9) Suntivich, J.; Gasteiger, H. A.; Yabuuchi, N.; Nakanishi, H.; Goodenough, J. B.; Shao-Horn, Y. *Nat. Chem.* **2011**, *3*, 546.

(10) Liang, Y.; Li, Y.; Wang, H.; Zhou, J.; Wang, J.; Regier, T.; Dai, H. *Nat. Mater.* **2011**, *10*, 780.

(11) Cao, R.; Thapa, R.; Kim, H.; Xu, X.; Kim, M. G.; Li, Q.; Park, N.; Liu, M.; Cho, J. *Nat. Commun.* **2013**, *4*, 2076.

(12) Chung, H. T.; Won, J. H.; Zelenay, P. *Nat. Commun.* **2013**, *4*, 1922.

(13) Gong, K.; Du, F.; Xia, Z.; Durstock, M.; Dai, L. *Science* **2009**, *323*, 760.

(14) Zhang, G.; Xia, B. Y.; Xiao, C.; Yu, L.; Wang, X.; Xie, Y.; Lou, X. W. *Angew. Chem., Int. Ed.* **2013**, *52*, 8643.

(15) Wu, Z.-S.; Yang, S.; Sun, Y.; Parvez, K.; Feng, X.; Müllen, K. *J. Am. Chem. Soc.* **2012**, *134*, 9082.

(16) Yang, W.; Fellinger, T.-P.; Antonietti, M. *J. Am. Chem. Soc.* **2010**, *133*, 206.

(17) Liu, J.; Sun, X.; Song, P.; Zhang, Y.; Xing, W.; Xu, W. *Adv. Mater.* **2013**, *25*, 6879.

(18) Ai, W.; Luo, Z.; Jiang, J.; Zhu, J.; Du, Z.; Fan, Z.; Xie, L.; Zhang, H.; Huang, W.; Yu, T. *Adv. Mater.* **2014**, *26*, 6186.

(19) Wang, Z.; Cao, X.; Ping, J.; Wang, Y.; Lin, T.; Huang, X.; Ma, Q.; Wang, F.; He, C.; Zhang, H. *Nanoscale* **2015**, *7*, 9394.

(20) Jasinski, R. *Nature* **1964**, *201*, 1212.

(21) Tang, H.; Yin, H.; Wang, J.; Yang, N.; Wang, D.; Tang, Z. *Angew. Chem., Int. Ed.* **2013**, *52*, 5585.

(22) Zagal, J. H. *Coord. Chem. Rev.* **1992**, *119*, 89.

(23) Zagal, J. H.; Griveau, S.; Silva, J. F.; Nyokong, T.; Bedioui, F. *Coord. Chem. Rev.* **2010**, *254*, 2755.

(24) Hijazi, I.; Bourgeteau, T.; Cornut, R.; Morozan, A.; Filoramo, A.; Leroy, J.; Derycke, V.; Jousselme, B.; Campidelli, S. *J. Am. Chem. Soc.* **2014**, *136*, 6348.

(25) Li, W.; Yu, A.; Higgins, D. C.; Llanos, B. G.; Chen, Z. *J. Am. Chem. Soc.* **2010**, *132*, 17056.

(26) Bashyam, R.; Zelenay, P. *Nature* **2006**, *443*, 63.

(27) Gupta, S.; Tryk, D.; Bae, I.; Aldred, W.; Yeager, E. *J. Appl. Electrochem.* **1989**, *19*, 19.

(28) Liang, J.; Zhou, R. F.; Chen, X. M.; Tang, Y. H.; Qiao, S. Z. *Adv. Mater.* **2014**, *26*, 6074.

(29) Tian, J.; Morozan, A.; Sougrati, M. T.; Lefevre, M.; Chenitz, R.; Dodelet, J.-P.; Jones, D.; Jaouen, F. *Angew. Chem., Int. Ed.* **2013**, *52*, 6867.

(30) Lin, L.; Zhu, Q.; Xu, A.-W. *J. Am. Chem. Soc.* **2014**, *136*, 11027.

(31) Zhao, Y.; Watanabe, K.; Hashimoto, K. *J. Am. Chem. Soc.* **2012**, *134*, 19528.

(32) Wu, Z.-S.; Chen, L.; Liu, J.; Parvez, K.; Liang, H.; Shu, J.; Sachdev, H.; Graf, R.; Feng, X.; Muellen, K. *Adv. Mater.* **2014**, *26*, 1450.

(33) Lefevre, M.; Proietti, E.; Jaouen, F.; Dodelet, J.-P. *Science* **2009**, *324*, 71.

(34) Wu, G.; More, K. L.; Johnston, C. M.; Zelenay, P. *Science* **2011**, *332*, 443.

(35) Serov, A.; Artyushkova, K.; Atanassov, P. *Adv. Energy Mater.* **2014**, *4*, 1301735.

(36) Wang, Q.; Zhou, Z.-Y.; Lai, Y.-J.; You, Y.; Liu, J.-G.; Wu, X.-L.; Terefe, E.; Chen, C.; Song, L.; Rauf, M.; Tian, N.; Sun, S.-G. *J. Am. Chem. Soc.* **2014**, *136*, 10882.

(37) Xiang, Z.; Xue, Y.; Cao, D.; Huang, L.; Chen, J.-F.; Dai, L. *Angew. Chem., Int. Ed.* **2014**, *53*, 2433.

(38) Zhao, S.; Yin, H.; Du, L.; He, L.; Zhao, K.; Chang, L.; Yin, G.; Zhao, H.; Liu, S.; Tang, Z. *ACS Nano* **2014**, *8*, 12660.

(39) Zhong, H.-X.; Wang, J.; Zhang, Y.-W.; Xu, W.-L.; Xing, W.; Xu, D.; Zhang, Y.-F.; Zhang, X.-B. *Angew. Chem., Int. Ed.* **2014**, *53*, 14235.

(40) Li, Z.; Li, G.; Jiang, L.; Li, J.; Sun, G.; Xia, C.; Li, F. *Angew. Chem., Int. Ed.* **2015**, *54*, 1494.

(41) Wu, G.; Zelenay, P. *Acc. Chem. Res.* **2013**, *46*, 1878.

(42) Ferrandon, M.; Kropf, A. J.; Myers, D. J.; Artyushkova, K.; Kramm, U.; Bogdanoff, P.; Wu, G.; Johnston, C. M.; Zelenay, P. *J. Phys. Chem. C* **2012**, *116*, 16001.

(43) Jaouen, F.; Lefevre, M.; Dodelet, J.-P.; Cai, M. *J. Phys. Chem. B* **2006**, *110*, 5553.

(44) Lefevre, M.; Dodelet, J. P.; Bertrand, P. *J. Phys. Chem. B* **2002**, *106*, 8705.

(45) Chen, R.; Li, H.; Chu, D.; Wang, G. *J. Phys. Chem. C* **2009**, *113*, 20689.

(46) Fellinger, T.-P.; Hasché, F.; Strasser, P.; Antonietti, M. *J. Am. Chem. Soc.* **2012**, *134*, 4072.

(47) Ramaswamy, N.; Tylus, U.; Jia, Q.; Mukerjee, S. *J. Am. Chem. Soc.* **2013**, *135*, 15443.

(48) Strickland, K.; Miner, E.; Jia, Q.; Tylus, U.; Ramaswamy, N.; Liang, W.; Sougrati, M.-T.; Jaouen, F.; Mukerjee, S. *Nat. Commun.* **2015**, *6*, 7343.

(49) Zitolo, A.; Goellner, V.; Armel, V.; Sougrati, M.-T.; Mineva, T.; Stievano, L.; Fonda, E.; Jaouen, F. *Nat. Mater.* **2015**, *14*, 937.

(50) Dodelet, J.-P. In *Electrocatalysis in Fuel Cells*; Springer: London, 2013; p 271.

(51) Olson, T. S.; Pylypenko, S.; Atanassov, P.; Asazawa, K.; Yamada, K.; Tanaka, H. *J. Phys. Chem. C* **2010**, *114*, 5049.

(52) Tylus, U.; Jia, Q.; Strickland, K.; Ramaswamy, N.; Serov, A.; Atanassov, P.; Mukerjee, S. *J. Phys. Chem. C* **2014**, *118*, 8999.

(53) Masa, J.; Zhao, A.; Xia, W.; Sun, Z.; Mei, B.; Muhler, M.; Schuhmann, W. *Electrochem. Commun.* **2013**, *34*, 113.

(54) Wang, L.; Ambrosi, A.; Pumera, M. *Angew. Chem., Int. Ed.* **2013**, *52*, 13818.

(55) Ai, K.; Liu, Y.; Ruan, C.; Lu, L.; Lu, G. *Adv. Mater.* **2013**, *25*, 998.

(56) Wen, Z.; Ci, S.; Zhang, F.; Feng, X.; Cui, S.; Mao, S.; Luo, S.; He, Z.; Chen, J. *Adv. Mater.* **2012**, *24*, 1399.

(57) Hu, Y.; Jensen, J. O.; Zhang, W.; Cleemann, L. N.; Xing, W.; Bjerrum, N. J.; Li, Q. *Angew. Chem., Int. Ed.* **2014**, *53*, 3675.

(58) Ding, W.; Li, L.; Xiong, K.; Wang, Y.; Li, W.; Nie, Y.; Chen, S.; Qi, X.; Wei, Z. *J. Am. Chem. Soc.* **2015**, *137*, 5414.

(59) Yang, W.; Liu, X.; Yue, X.; Jia, J.; Guo, S. *J. Am. Chem. Soc.* **2015**, *137*, 1436.

(60) Proietti, E.; Jaouen, F.; Lefèvre, M.; Larouche, N.; Tian, J.; Herranz, J.; Dodelet, J.-P. *Nat. Commun.* **2011**, *2*, 416.

(61) He, Z.; Maurice, J.-L.; Gohier, A.; Lee, C. S.; Pribat, D.; Cojocaru, C. S. *Chem. Mater.* **2011**, *23*, 5379.

(62) Yoshida, H.; Takeda, S.; Uchiyama, T.; Kohno, H.; Homma, Y. *Nano Lett.* **2008**, *8*, 2082.

(63) Rodríguez-Manzo, J. A.; Terrones, M.; Terrones, H.; Kroto, H. W.; Sun, L.; Banhart, F. *Nat. Nanotechnol.* **2007**, *2*, 307.

(64) Zhang, J. *PEM Fuel Cell Electrocatalysts and Catalyst Layers: Fundamentals and Applications*; Springer, 2008.

(65) Li, Y.; Zhou, W.; Wang, H.; Xie, L.; Liang, Y.; Wei, F.; Idrobo, J.-C.; Pennycook, S. J.; Dai, H. *Nat. Nanotechnol.* **2012**, *7*, 394.

(66) Yang, J.; Liu, D.-J.; Kariuki, N. N.; Chen, L. X. *Chem. Commun.* **2008**, 329.

(67) Niwa, Y.; Kobayashi, H.; Tsuchiya, T. *Inorg. Chem.* **1974**, *13*, 2891.

(68) Thorum, M. S.; Hankett, J. M.; Gewirth, A. A. *J. Phys. Chem. Lett.* **2011**, *2*, 295.

(69) Deng, D.; Yu, L.; Chen, X.; Wang, G.; Jin, L.; Pan, X.; Deng, J.; Sun, G.; Bao, X. *Angew. Chem., Int. Ed.* **2013**, *52*, 371.

(70) Lee, J.-S.; Park, G. S.; Kim, S. T.; Liu, M.; Cho, J. *Angew. Chem., Int. Ed.* **2013**, *52*, 1026.

(71) Faubert, G.; Lalande, G.; Côté, R.; Guay, D.; Dodelet, J. P.; Weng, L. T.; Bertrand, P.; Dénès, G. *Electrochim. Acta* **1996**, *41*, 1689.